CrossMark

ORIGINAL PAPER

Particulate modeling of cementation effects on small and large strain behaviors in granular material

Z. Ning[1] · A. Khoubani[2] · T. M. Evans[2]

Abstract Most previous studies of cemented sands have focused on quantifying response at either the element scale or the field scale based on laboratory or in-situ test results. These studies provide important practical information about the engineering behavior of cemented sands, but often generate little knowledge about the underlying physics that governs the response at readily observable physical scales. The current study seeks to provide some insight into the particle-level mechanics of cemented sands through the use of discrete element method simulations that have been calibrated to a test bed of physical results previously reported in the literature. Numerical particle assemblies are subjected to applied boundary stresses and evolutions in bond breakage, shear wave velocity, assembly fabric, and contact forces are observed. Important similarities and differences in the load-carrying response of bonded and unbonded granular materials are observed and quantified. Shortcomings of traditional approaches to modeling cemented sands are identified.

1 Introduction

Cementation can occur naturally in soils due to the precipitation of certain minerals such as salts, iron oxides, and calcite [25,35] or artificially by using cementing agents such as lime,

✉ T. M. Evans
matt.evans@oregonstate.edu

[1] SIXENSE - USA/Canada Area, 1448 Elliott Ave. W., Seattle, WA 98119, USA

[2] School of Civil and Construction Engineering, Oregon State University, 101 Kearney Hall, Corvallis, OR 97331, USA

ordinary Portland cement, and gypsum. There are also novel artificial soil improvement techniques such as microbially induced calcite precipitation (MICP, [7,27]) which mimics the natural cementation process.

The improved engineering properties of cemented soils with regards to both large-strain and small-strain responses have been recognized and studied. Large-strain behavior of cemented soils are usually studied under drained or undrained triaxial compression (e.g., [1,22]) and K_0 compression (e.g., [49]). Previous studies show an increasing degree of cementation produces increasing peak shear strength and dilative volumetric response. Studies of small-strain response in cemented soil primarily focus on small-strain shear modulus and damping ratio. Small-strain shear modulus is correlated to shear (S-) wave velocity and is normally assessed using either the resonant column test [1,15,37] or bender element test [7,27,29,30,49]. It has been shown that small-strain shear modulus is increased by cementation due to the enlarged contact area between particles [15]. There have also been studies aimed at correlating small-strain properties to large-strain properties for cemented soils. Saxena and Lastrico [36] developed a correlation between small-strain modulus and static strength under a particular confining pressure. Sharma et al.[39] proposed a relationship between S-wave velocity and stresses at failure based on drained triaxial compression tests on weakly cemented sands.

While most of these above-mentioned studies are experimental and emphasize macroscale behaviors, there has been increasing numerical work aimed at exploring the underlying mechanisms which control the behaviors of cemented soils. Initial discrete element method (DEM) work in this area was conducted by Trent and Margolin [41]. Wang and Leung [43,44] studied the evolution of decementation, contact force chains, and shear band formation using two-dimensional DEM simulations. Similar DEM simulations

were conducted by Jiang et al. [19], focusing on the effects of bonding model and the parameters used to simulate the cementing agent on large-strain response of cemented specimens to biaxial compression. As for numerical studies on small-strain response, Sadd et al. [34] showed that the wave speed in a two-dimensional DEM assembly is very sensitive to the cementation fabric distribution and is higher than the uncemented case. Evans and Ning [11] measured S-wave velocity on three-dimensional DEM models subjected to various load-cementation histories and reported decreasing S-wave velocity associated with decementation when the specimen was subjected to isotropic unloading.

This paper explores the effects of cementation on both the small-strain and the large-strain behaviors of cemented granular assemblies using three dimensional DEM simulations. Special emphasis is placed on the analysis of decementation during different loading conditions since the direct measurement of the amount of cementation is extremely difficult in physical experiments [26]. The simulation of cementing agent, S-wave generation, and response measurement are presented first. The basic model parameters are calibrated based on experimental results by Sharma et al. [39]. Then the effects of cement content, confining stress and two distinct load-cement histories on S-wave velocity under isotropic consolidation are shown and discussed. Finally the stress–strain and volumetric response, and the evolution of S-wave velocity during drained triaxial test of cemented specimens are presented and compared to experimental results [39]. Microscale analysis is highlighted in regard of bond network, normal contact force, local porosity, and local coordination number.

2 The discrete element model

2.1 Geometry and loading

A diameter (D) to height (H) ratio of 1.5 was selected for the numerical specimen to minimize the P-wave reflection from specimen boundaries which is commonly observed in typical triaxial samples with a (D/H) ratio of 0.5 [24,29]. Ning et al. [30] showed that when the specimen lateral boundaries are sufficiently distant, the zone along the central axis of the specimen where the receivers are located is less affected by P-wave interference. The numerical specimens consisted of over 52,000 spherical particles with the grain size distribution shown in Fig. 1. A large number of particles is critical for obtaining repeatable simulation results, particularly for S-wave measurement. Mass scaling was used to speed up the numerical simulation. Particles' radius was increased 1000 times while the density was kept constant. Ning et al. [30] showed that increase of particle size decreases the resonant frequency of specimen but does not change the shear
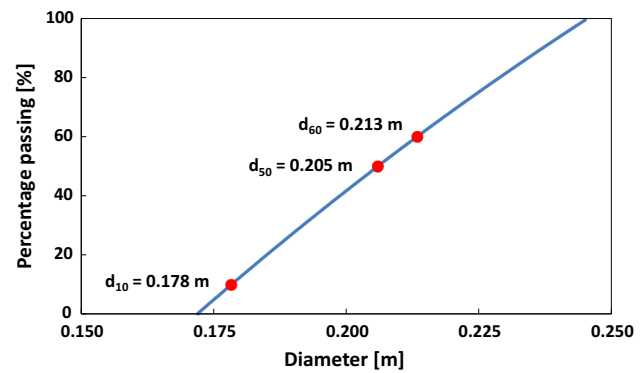

Fig. 1 Specimen's grain size distribution

wave velocity. A flexible membrane was modelled using the stacked cylindrical wall algorithm [13,51] to provide lateral confinement for the assembly of particles. This stacked-wall boundary is computationally economical relative to other published flexible membrane simulation methods and has been proven capable of effectively capturing stress–strain–volume change response in discrete element simulations [51]. Rigid planar walls were employed to constrain the top and bottom of the assembly. Isotropic consolidation was accomplished by servo-controlling the translational velocities of the top and bottom rigid walls and the radial velocities of the stacked cylindrical walls. The average contact forces between the particles and the walls were constantly checked to adjust the wall velocities so as to maintain the target isotropic confining stress. At the end of consolidation, triaxial compression was simulated by moving the bottom and the top rigid walls towards each other at a constant rate while servo-controlling the radial velocities of the stacked cylindrical walls to maintain the desired confining stress.

2.2 Contact and bonding models

Interaction between particles was simulated using the Hertz-Mindlin contact model (e.g., [20,23]). Viscous damping is introduced at the contact points between particles to avoid non-physical vibrations in the model. Normal and shear viscous damping generate forces at the contact point between two particles that are proportional to the particles relative velocity in the corresponding direction. This type of viscous damping model is appropriate for non-collisional regimes, as all the simulations in this study include small strain perturbations due to shear wave propagation and quasi-static large deformations in triaxial compression test. For collision problems more appropriate damping models can be used [21]. Cementation is simulated via parallel bonds between particles. Parallel bonds transmit normal forces, shear forces, and moment at the contact point by providing normal and shear stiffnesses that act in parallel with the stiffnesses defined
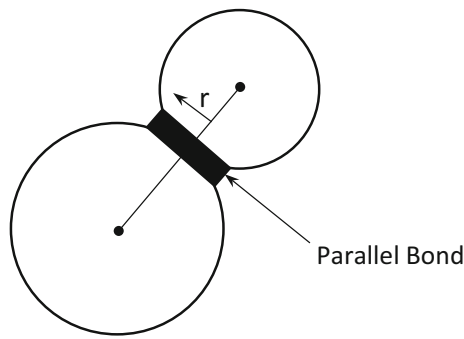
Fig. 2 Schematic view of parallel bonding model (after [18])

Table 1 Basic material parameters used in the DEM simulation

Parameters	Value
Particle properties	
Specific gravity, G_s	2.65
Shear modulus, G_g	2.9×10^9 Pa
Poisson's ratio, υ_g	0.31
Interparticle friction, μ	0.31
Mean particle diameter, D_{50}	0.205 m
Uniformity coefficient, C_u	1.2
Bond properties	
Normal stiffness	5×10^8 N/m
Shear stiffness	1×10^9 N/m
Normal strength	5×10^6 Pa
Shear strength	5×10^6 Pa
Specimen geometry	
Specimen diameter/D_{50}	43.9
Specimen height/D_{50}	29.3

by the contact model [31]. Cementation in granular materials involves changes in the surface texture of the individual grains, changes in fabric, the formation of inter-particle bonds, and thus, changes in the internal distribution of contact forces [15]. Though a parallel bond does not reproduce all of the aforementioned cementation effects, it does mimic the inter-particle bond effect of real cementation by providing a connection between two particles that transmits both forces and moments, as shown in Fig. 2. The basic particle and parallel bond properties were calibrated based on physical tests as discussed subsequently in Sect. 4 and are listed in Table 1.

2.3 Shear wave generation and measurement

Shear (S-)wave velocity was measured in the granular assemblies to evaluate the effects of cementation on small-strain behavior. S-waves were generated by applying a horizontal excitation (along the x-axis) to a thin layer of particles at the
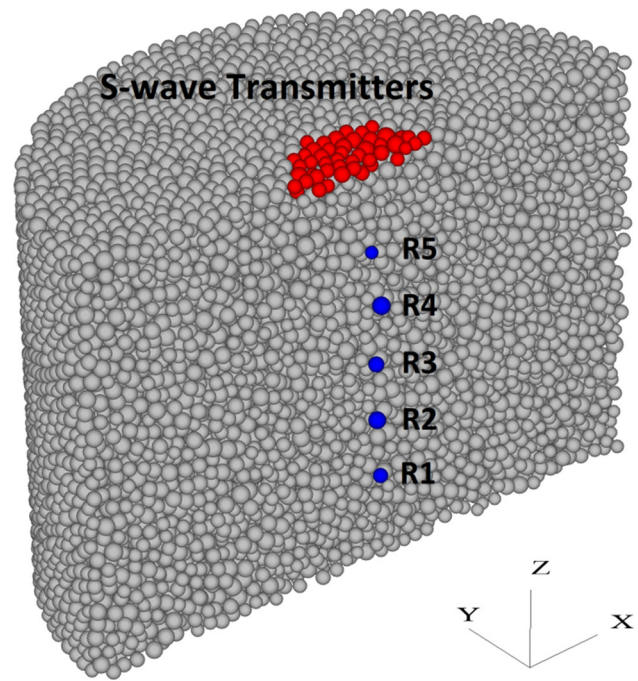

Fig. 3 A typical DEM specimen with S-wave transmitting zone and receivers. For clarity, only half of the specimen is shown. *Red particles* S-wave transmitters; *blue particles* S-wave receivers (color figure online)

top of the specimen using a single sinusoidal velocity pulse (Fig. 3). The diameter of this S-wave transmitting zone is $D/4$ (D = specimen diameter) and its thickness is nominally $2 \times D_{50}$. Compared to the S-wave generation in bender element tests, in which the wave source is approximately a point and the wave propagation front is spherical, this approach reduces the P-wave interference effect [24] observed in physical specimens [29,30]. The DEM model was excited by sine pulses of different frequencies to obtain the resonant frequency of the specimen. In subsequent simulations, the excitation frequency was selected close to the resonant frequency to obtain a strong response in the model. In DEM simulations, the displacement and velocity of each individual particle is known, so five approximately equally spaced particles along the central axis of the cylindrical specimen were selected (R1 through R5) to monitor particle motions during wave propagation.

Figure 4 shows source and receiving signals from a typical DEM simulation. The amplitude of the signal is a representation of the displacement of particles in the direction of the excitation (normalized by the amplitude of the source signal). It can be seen that the receivers respond to the excitation at different times. The delays between the equally spaced receivers are almost the same. The receiving signals have identical waveforms but attenuate as the distance to the source increases. The S-wave velocities were determined by first calculating the travel times and distances between
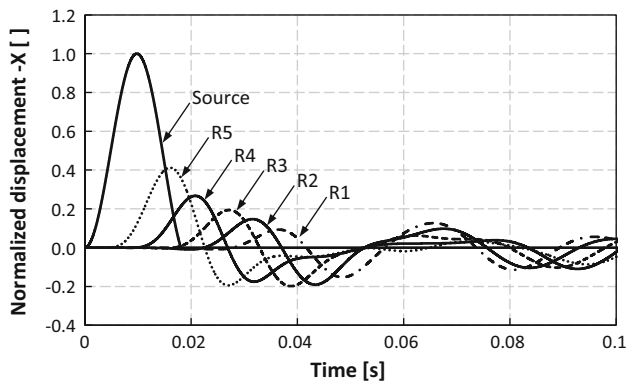
Fig. 4 Source and receiver signals for shear wave velocity calculations

each of the neighboring receiver pairs using the start-to-start method [48] and then averaging the resulting wave velocities. Care also should be taken regarding the excitation amplitude of source particles, as a large amplitude can lead to inelastic deformation in the assembly. The adequacy of the excitation amplitude was investigated by Ning et al. [30] where several shear waves were applied to an assembly of un-cemented particles and receiver response was shown to be the same for repeated application of shear waves.

3 Parametric study of parallel bond behavior

Parallel bond behavior is specified by normal and shear stiffness, normal and shear strength, and bond radius (necessary for computing moments and calculating stresses from forces). When the magnitude of the normal or shear stress exceeds the respective strength, the bond breaks. No slip is possible at the contact while the bond remains intact. Results of parametric analyses are presented in Fig. 5 and show the effects of bond parameters on the stress–strain behavior of cemented specimens subjected to triaxial compression. In Fig. 5, all of the bond parameters are normalized by the base parameters listed in Table 1 ($\{k_n\}$: normalized normal stiffness; $\{k_s\}$: normalized shear stiffness; $\{s_n\}$: normalized normal strength; $\{s_s\}$: normalized shear strength). In Fig. 5a, it can be seen that increasing the bond normal stiffness increases the specimen stiffness without significantly changing its shear strength. In Fig. 5b, the specimen becomes stiffer as bond shear stiffness is increased. The shear strength of the specimen first increases when bond shear stiffness is increased from a relatively low value, but decreases as response becomes very brittle with continuing increases in bond shear stiffness. Comparing Fig. 5a and b, the bond shear stiffness shows more significant effects than the bond normal stiffness. In Fig. 5c, d, the specimen shear strength is improved by increasing the bond strength but the initial stiffness of the specimen is not affected by either the bond normal

strength or the bond shear strength. Changing the bond shear strength shows a more significant effect than changing the bond normal strength, implying the majority of bonds are failing in shear for the baseline parameters.

4 Model calibration

The base particle and parallel bond parameters were determined through calibration of model response to deviatoric stress–axial strain data from drained triaxial compression tests at 100 kPa confining pressure reported by Sharma et al. [39] on uncemented and weakly cemented quartz sand with 1, 2.5 and 5% cement content (cc). Ordinary Portland cement (OPC) was used as the cementing agent in the tests. Particle parameters (shear modulus, Poisson's ratio, and interparticle friction) were calibrated to the laboratory results for the uncemented specimen. Then using the calibrated particle parameters, the parallel bond normal/shear stiffness and normal/shear strength were calibrated based on the test data from the 5% cc specimen. Using the known cement content by weight (i.e., 5%), the bond radius (a direct measure of cement volume) was calculated based on the specific gravity of the particles (2.65) and the cementing agent (3.15), the mean particle diameter (D_{50}), and average coordination number (CN; the average number of contacts per particle). Bonds were installed at all particle-particle contacts. Then for 2.5% cement and 1% cement cases, the same bond parameters were used except for the bonds were installed at 50 and 20% of the contacts (uniformly distributed within the DEM specimen), respectively, resulting in cement contents consistent with the laboratory specimens. Bond radius was kept constant for all simulations. If cement content were varied in some other way (e.g., by varying bond radius), we would expect slightly different, yet still internally consistent, results. This approach results in good predictions of the stress–strain curves for laboratory tests. These basic particle and parallel bond parameters are presented in Table 1. Some of these properties were subsequently varied as part of parametric studies. It is noted that in the current 3D DEM simulations, the calibrated bond normal/shear strength used are similar to those used in previous 2D DEM studies on cemented sand [19,43,44].

The deviatoric stress versus axial strain curves and the volumetric strain versus axial strain curves of the calibrated DEM specimens with various cement contents under triaxial compression are shown in Fig. 6. It is readily observed that: (a) increasing cement content produces higher peak shear strength and results in a more brittle response (i.e., sharp decrease in deviatoric stress after reaching some peak value, indicating a considerable difference between the peak and residual strengths); (b) specimens with higher cement contents experience greater dilation. These observations are
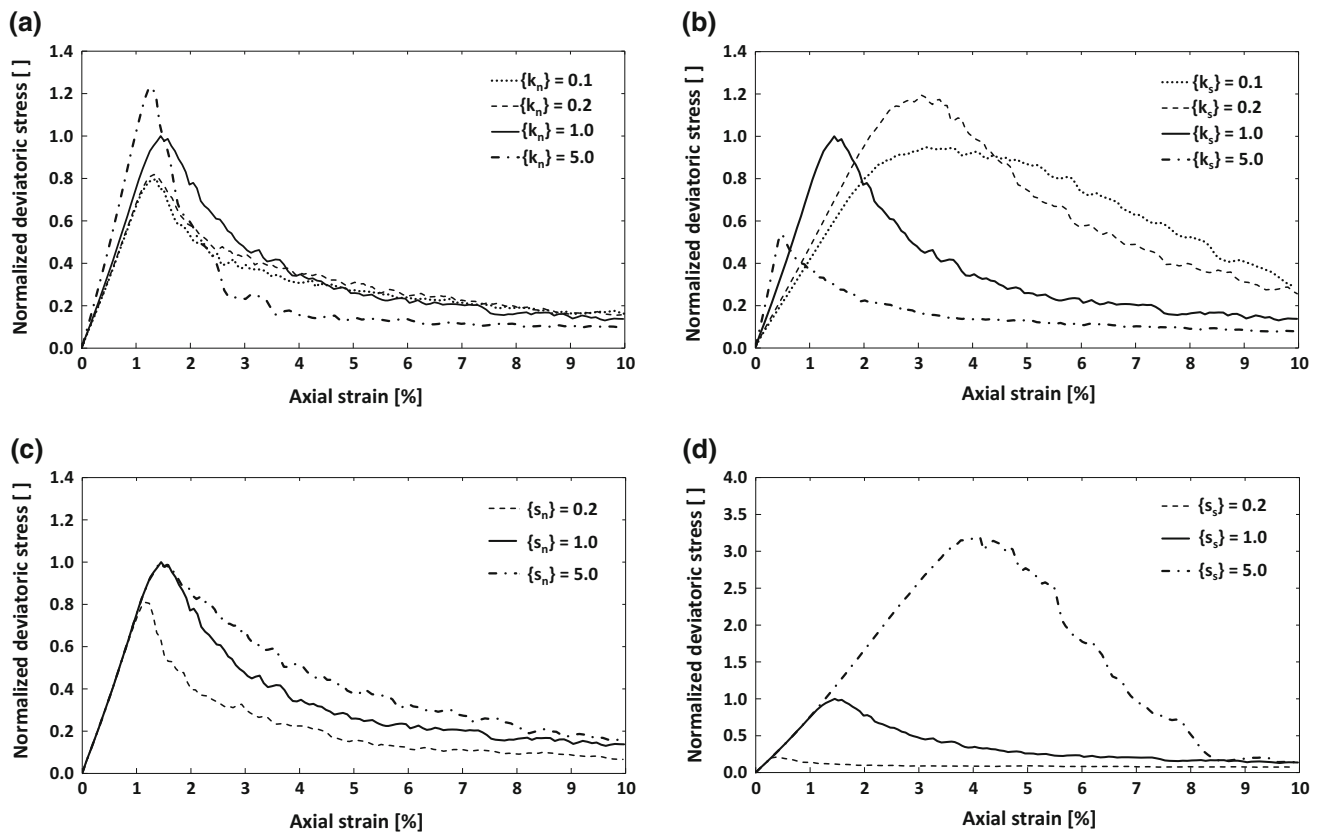
Fig. 5 Parametric study of parallel bond parameters. **a** Bond normal stiffness; **b** bond shear stiffness; **c** bond normal strength; **d** bond shear strength. Deviatoric stress is normalized by the peak deviatoric stress produced in the specimen with the baseline parameters

consistent with the findings in other experimental and numerical studies on cemented soils (e.g., [1,19]). It should be noted that Sharma et al. [39] reported contractive behavior for the uncemented and 1% cc specimens, but in the current simulation, with the particle and bond parameters calibrated to the deviatoric stress versus axial strain curves, they show dilative behaviors but are less dilatant than specimens with higher cement contents. Many studies in the literature contain instances of DEM results which overpredict dilations measured in the laboratory (e.g., [9,40,51]). This difference is due to the imperfect simulation of compliant confinement provided by stacked walls boundaries (though these are a significant improvement over single-cylinder confinement); (c) critical state shear strength is the same for different cement contents. Some prior experimental studies (e.g., [38,39]) found that critical state shear strength was dependent on cement content while other studies (e.g., [43,44]) showed the existence of a unique critical state regardless of the level of cementation. It is expected that in laboratory tests the cement content should have an effect on critical state. Cementation changes the surface texture of individual grains, increasing interparticle friction, and bond breakage results in the generation of silt-sized fines that will fill pores in the sand matrix. Parallel bonds, however, do not model these features.

5 Effects of cementation history: isotropic loading

Confining stress, cement content, and the load-cementation history are the main factors that affect the small-strain stiffness of cemented soils [11,15,27]. The two distinct load-cementation histories are: loading before cementation (LBC) and cementation before loading (CBL). The first case is common in natural deposits, where materials are compressed by the weight of overburden deposits followed by diagenetic cementation processes. The second case reflects the common procedure for preparation of artificially cemented specimens in the laboratory [37,39]. In the current simulations, cemented specimens were isotropically consolidated to various levels of confining stress under LBC and CBL cementation histories. In LBC cases, the specimens were first isotropically consolidated to the target confining stress. Then the bonds were installed. Finally the S-wave velocity was measured. In CBL cases, the bonds were installed when the specimens was consolidated to 10 kPa isotropic confining stress. Then the specimens were further isotropically consolidated to the same target confining stress as in the LBC cases. Finally, the S-wave velocity was measured. The simulated testing program is described in Table 2.
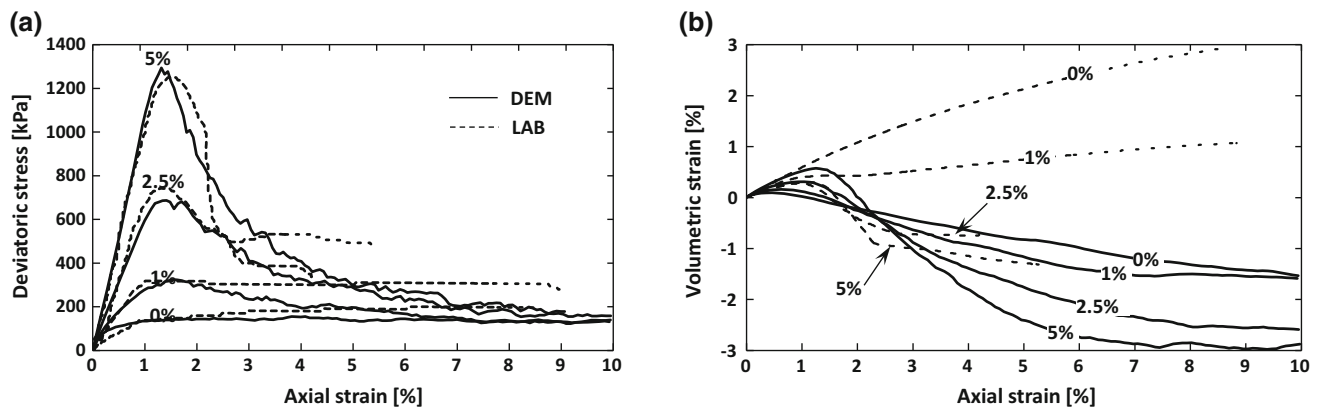
(a)

(b)

Fig. 6 Comparison of calibrated numerical model response to stress–strain–volume change behavior measured in triaxial compression: **a** deviatoric stress versus axial strain; **b** volumetric strain versus axial strain. Confining stress = 100 kPa.

Table 2 Simulated testing program

Cementation history	Cement content (%)	Isotropic stress (kPa)	Fitting parameters	
			α (m/s)	β
Uncemented	0	100, 300, 600, 900, 1200	68.8	0.187
Loading before cementation (LBC)	1	100, 300, 600, 900, 1200	79.3	0.169
	2.5		85.6	0.165
	5		96.1	0.151
Cementation before loading (CBL)	1	100, 300, 600, 900, 1200	70.7	0.188
	2.5		77.8	0.180
	5		90.0	0.168

Figure 7 shows the variation of S-wave velocity under different confining stresses for specimens with different cement contents. Several observations can be made. Clearly, S-wave velocity increases as the degree of cementation increases. However, this effect is less significant when compared to the physical tests [1,39]. For example, in the current simulation, the S-wave velocity is increased by only 20% for 5% cc case while in Sharma's experiment a 180% increase in S-wave velocity was reported for the same cement content.

S-wave velocity also increases as the confining stress increases. For both uncemented and cemented cases, the S-wave velocity is shown to be a power function of confining stress, which can be fitted using the general equation $V_s = \alpha(\sigma/1\,\text{kPa})^{\beta}$, where α and β are the fitting parameters shown in Table 2. It is noted that the β values slightly decrease as the cement content increases but all are around 1/6, which is the theoretical value for particulate media with Hertzian contacts at moderate stress levels [3,4,8,16,17,42]. The constant β values for specimens with various cement contents are consistent with the findings in [1] for Monterey No. 0/30 sand. However, according to many recent studies [15,27], in the *cementation-controlled* region [35], where the cementation degree is relatively high and the confining stress

is relatively low, the β value is close to zero, implying the S-wave velocity is minimally sensitive to the stress state—i.e., so-called *rock-like* behavior [27].

There is very small variation of S-wave velocity between LBC and CBL cases. This agrees with the experimental results of Fernandez and Santamarina [15]. The small variation between the measured S-wave velocity for LBC and CBL cases with the same cement content implies that the level of cementation is significantly more important than the stress-cementation history. The LBC case produced lower β values than the CBL case, which indicates the small-strain stiffness in LBC cemented specimens is less sensitive to stress state. This is due to the geometry of the Hertzian contact model (i.e., contact radius increases nonlinearly with increasing normal force) because a larger particle-particle contact area will develop for particles loaded before being cemented. Therefore, further increases in confining stress result in smaller increases of contact area and thus, smaller gains in interparticle stiffness (i.e., contact quality, [10,50]).

The discrepancies in the increase in S-wave velocity due to cementation and its sensitivity to stress state for the current simulations and previous experimental studies are likely due to the fact that the parallel bond used in the simulation
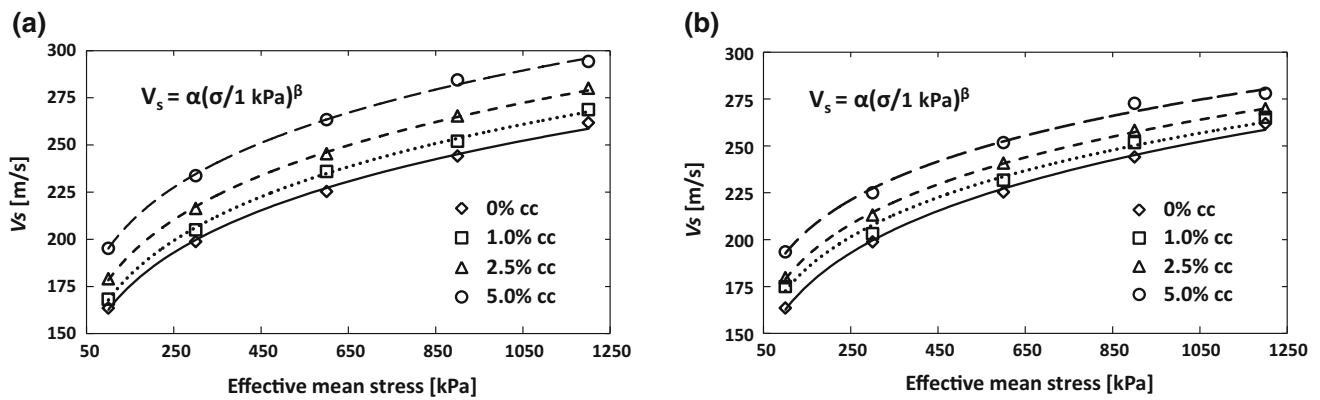
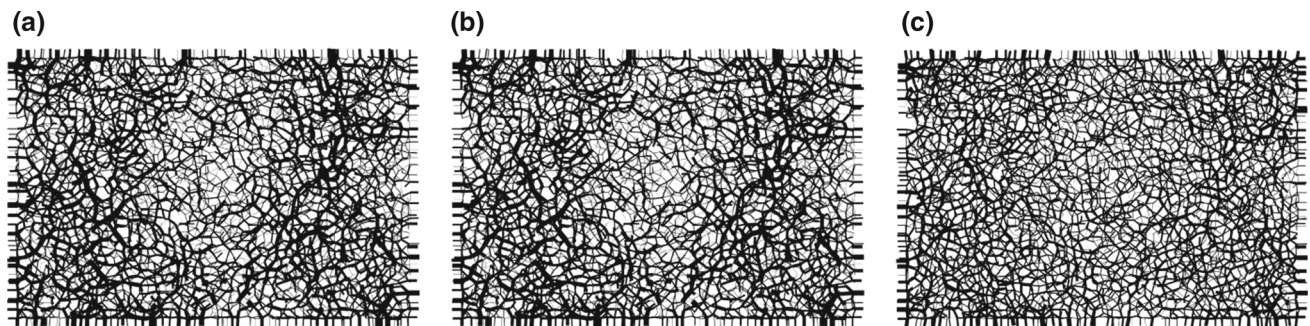**Fig. 7** S-wave velocity versus confining stress under isotropic consolidation: **a** LBC; **b** CBL

Fig. 8 Normal contact forces on the xz-plane: **a** uncemented; **b** 5% cc LBC; **c** 5% cc CBL specimens at 1200 kPa isotropic stress
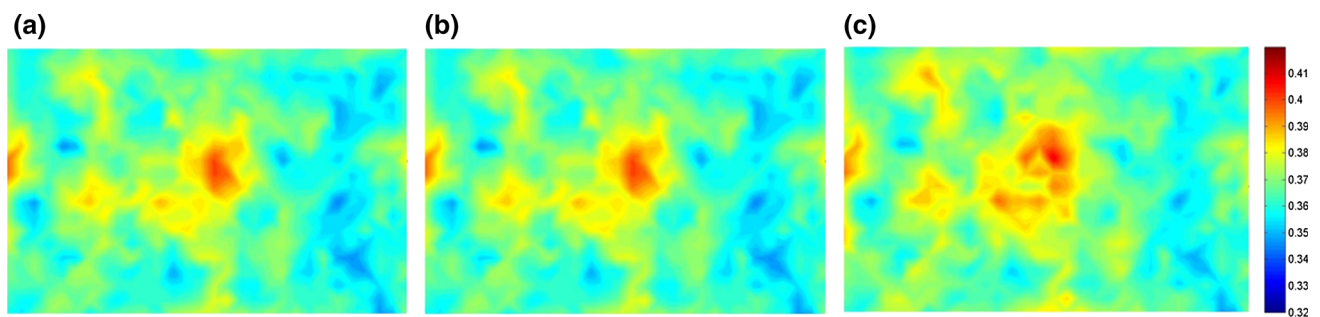

Fig. 9 Porosity contours on the xz-plane: **a** uncemented; **b** 5% cc LBC; **c** 5% cc CBL specimens at 1200 kPa isotropic stress

is simply a mathematical construct that enhances the tensile and shear resistance at a contact but is not a real physical substance (i.e., it does not increase the contact area between particles). In real soil, the effective contact is much larger because of the cementing agent. This is a topic that is currently the subject of active research [12].

Though specimens with different cementation-loading histories produce very similar S-wave velocities, the following analysis shows the differences between these two cases from a microscale perspective. The normal contact force chains, porosity contours and coordination number contours on an xz plane passing through the specimen axis of symmetry for 0% cc, 5% cc LBC and 5% cc CBL cases at 1200 kPa confining stress are shown in Figs. 8, 9 and 10. Porosity and

coordination number are calculated for 600 spherical regions of diameter $8 \times D_{50}$ with their centroids on the cutting plane. Contours are then generated using a simple kriging algorithm in MATLAB.

Figure 8 shows very similar normal contact force chains for the 5% cc LBC and uncemented cases. In both instances, a weak contact force area can be seen in the core zone and is surrounded by strong contact force chains. This particular pattern of normal contact force is developed because the fabric of the particulate assembly adjusts to react to the external force. For the uncemented and LBC cases, when the confining stress is gradually increased without the help of any bonding force, translational and rotational movement of particles occurs to form the particular arch-like microstructure
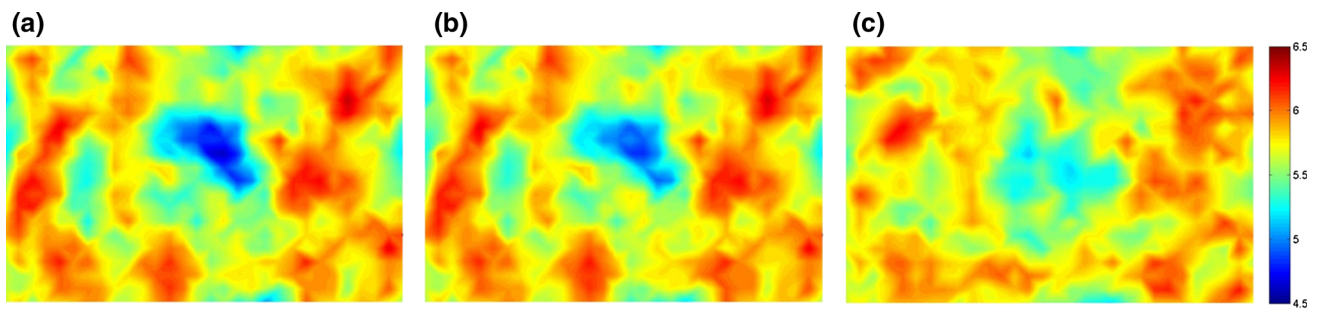
Fig. 10 Coordination number contours on the xz-plane: **a** uncemented; **b** 5% cc LBC; **c** 5% cc CBL specimens at 1200 kPa isotropic stress
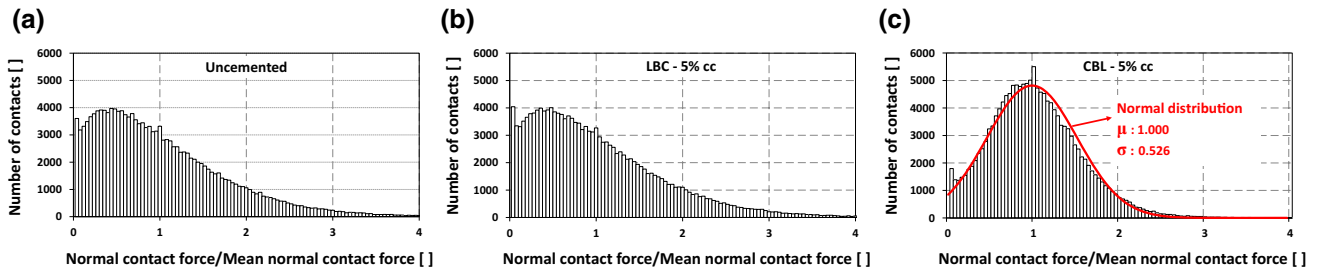

Fig. 11 Histograms of normal contact forces: **a** uncemented; **b** 5% cc LBC; **c** 5% cc CBL specimens at 1200 kPa isotropic stress

to resist the isotropic confining stress in the most efficient way. For the CBL case, the normal contact force distribution is more uniform because the bonds increase the interparticle shear resistance, which prevents interparticle movements. The distributions of normal contact force for the uncemented, LBC and CBL cases are quantified using force histograms, as shown in Fig. 11. It can be seen that the uncemented and the LBC case have very similar contact force distributions. The contact force distribution for the CBL case is similar to a (one-side truncated) normal distribution, consistent with the visual observation of Fig. 8 that shows a high concentration of contacts with similar normal force. A normal distribution curve with the mean (μ) and standard deviation (σ) values of the normal contact forces is plotted on the force histogram in Fig. 11c to illustrate this fact. Qualitatively, the agreement between the normal distribution and the histogram is reasonable. It has been shown previously that high confining stresses cause breakdown of cementation [2], so arch-like force chains are also expected to develop in the CBL specimen if the confining stress is further increased. In the current simulation, only 0.38% bond breakage occurs under 1200 kPa confining stress.

The distributions of porosity and coordination number shown in Figs. 9 and 10 respectively are consistent with the contact force distribution. In general, low porosity and high coordination number are observed in the areas with concentrated high contact forces while high porosity and low coordination number are seen mainly in the core zone where contact forces are low. Again, the LBC and uncemented specimens have similar porosity and coordination number

distributions. Distinctions between the LBC and CBL specimens are less obvious from the porosity distribution but are well demonstrated in terms of the coordination number distribution. For the LBC case, low CN concentration is well identified in the core zone for the same reason that the arch-like contact force chain is formed surrounding the core. For the CBL case, the spatial variation of coordination number is less prominent.

6 Specimen response in axisymmetric compression

The effects of cementation on both large-strain and small-strain response are studied for specimens subjected to axisymmetric compression. The relationship between cement degradation and stress–strain response, volumetric behavior, shear band formation and S-wave velocity are particularly investigated. A LBC specimen at 100 kPa confining stress is considered.

6.1 Particle, void, and fabric behaviors

Figure 12 presents deviatoric stress, volumetric strain, bond breakage, and S-wave velocity evolution versus axial strain. System response is divided into four zones based on the observed stress–strain behavior: Zone I, from the start of the test to yield ($\varepsilon_a = 0-1.1\%$); Zone II, from yielding to peak strength ($\varepsilon_a = 1.1-1.5\%$); Zone III, from peak strength to approaching a steady state ($\varepsilon_a = 1.5-6.5\%$); and Zone IV, from the beginning of the steady state to the
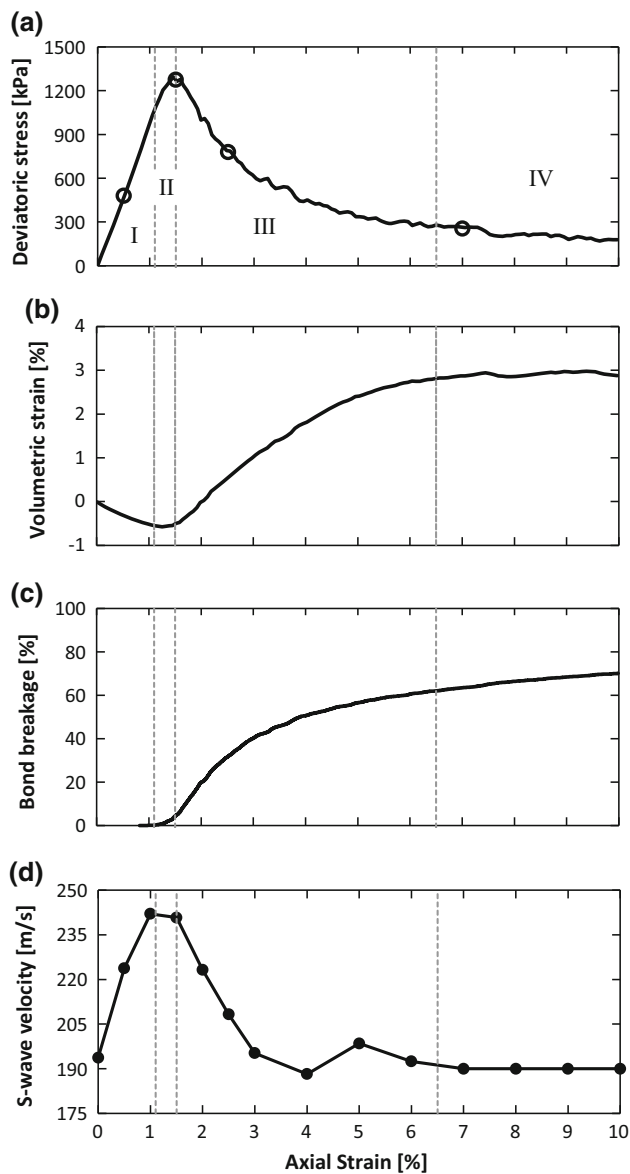
Fig. 12 Stress–strain response, volumetric response, bond breakage history, and S-wave evolution of 5% cc specimen under 100 kPa confining stress

steady state when bond breakage slows down to a minimal rate. Similar observations on the correlation between bond breakage and cemented sand behaviors were previously reported in two-dimensional DEM biaxial test simulations (e.g. [19]).

Microscale analyses were performed to provide further insight into the mechanisms of bond breakage effects on cemented specimen behavior under triaxial compression. Figure 13 shows the evolution of normal contact forces, the bond network, local porosity, and local coordination number at four axial strain levels falling in each of the four characteristic zones (on the xz plane). It is apparent that, at $\varepsilon_a = 0.5\%$, well before yielding, the bond network remains intact. The normal contact forces are uniformly distributed without forming dominant force chains. Relatively high local porosities and low coordination numbers are observed in the central area due to the initial isotropic consolidation effect before triaxial compression, as discussed previously. At $\varepsilon_a = 1.5\%$, where peak strength is reached, minimal bond breakage can be observed. Dominant force chains are propagating vertically through the specimen. No significant change in local porosity is evident, while local coordination numbers decrease on the lateral edges of the specimen. At $\varepsilon_a = 2.5\%$, where deviator stress has rapidly dropped and the specimen is dilating, significant bond breakage can be observed, forming an 'X' shaped bond breakage zone. Local force-chain buckling occurs near the top and the bottom of the specimen with contact forces concentrated in the center. Incongruously, both local porosity and coordination number increase simultaneously in the bond breakage zone. At $\varepsilon_a = 7\%$, where the specimen is approaching a steady state, the 'X' shaped bond breakage zone expands while little new breakage occurs within the intact zone. Many of the contact force chains break down and the contact forces become highly concentrated in the center of the specimen, accompanied by continued increase in coordination number. Dilative shear bands can be clearly identified from the porosity contours. It should be noted that the application of stacked-wall cylindrical confinement in conjunction with the top and bottom parallel platens results in enforced axisymmetric deformation of the specimen. This manifests as the 'X' shaped bond breakage zone and shear bands; however, in physical experiments only one of the two failure planes often occurs (e.g., [14]).

6.1.1 Contact force

Summary statistics for normal contact forces at the strain levels considered in Fig. 13 are presented in Table 3. The mean contact force reflects the specimen scale stress–strain response: it first increases and then gradually decreases. However, the maximum contact force increases monotonically, implying the development of high locked-in contact

end of the test ($\varepsilon_a = 6.5-10\%$). Volumetric strain also shows distinct behaviors in these four zones (Fig. 12b). Zone I shows volumetric contraction. Zone II is a transition zone from contraction to dilation. Significant dilation is developed in Zone III. In Zone IV, the volumetric strain is almost constant, implying a steady state. Observing bond breakage versus applied strain reveals the underlying correlations between cement degradation and specimen-scale behavior. In Fig. 12c, it can be seen that specimen yield and volumetric dilation occurs at the onset of bond breakage. Decreasing deviatoric stress and significant dilation is associated with dramatic bond breakage. The specimen is approaching a
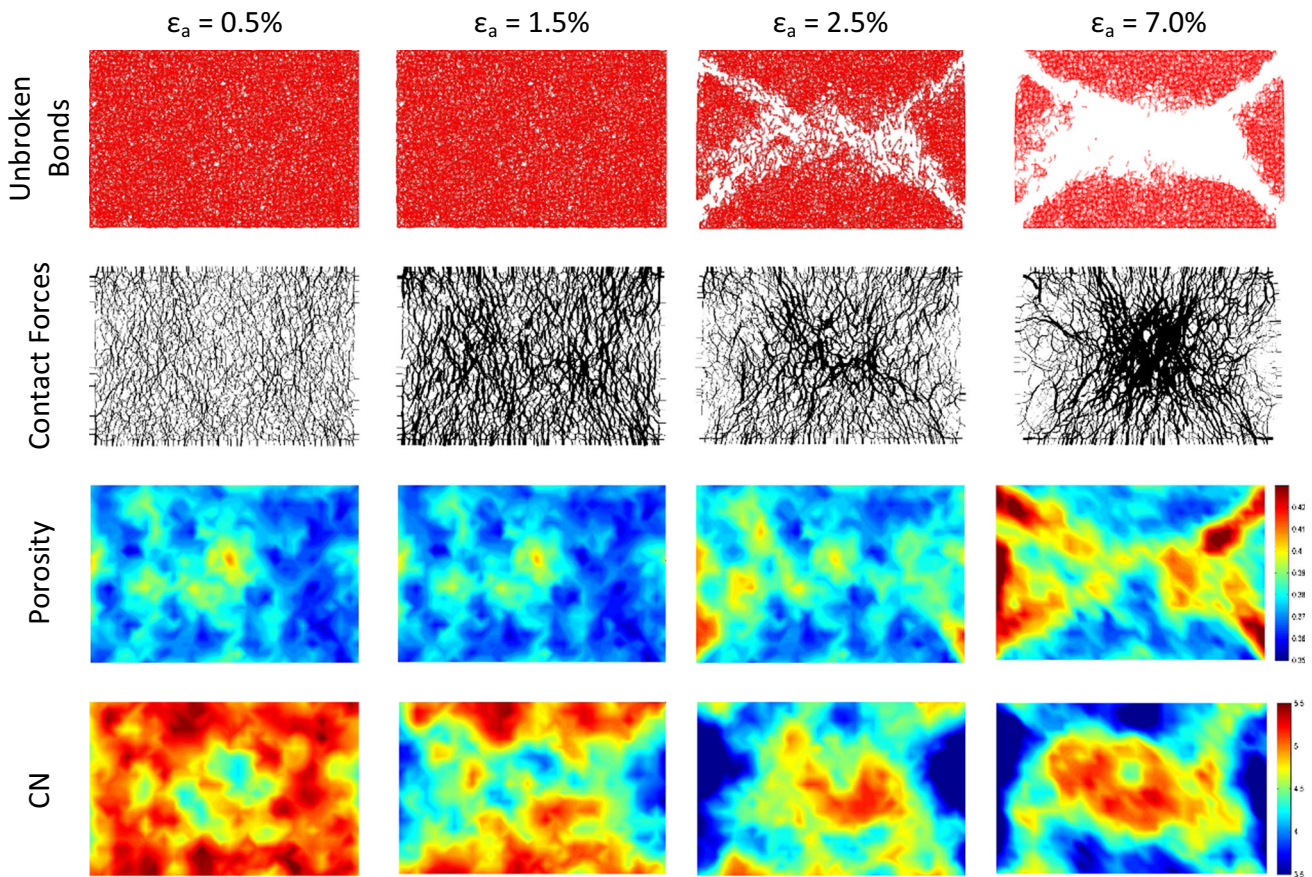
Fig. 13 Evolution of internal structure during shear

Table 3 Statistics of normal contact force for 5% cc specimen under triaxial compression

Strain level (%)	Max (N)	Min (N)	Mean (N)	Std. deviation (N)	COV
0.5	1.25×10^5	6.45×10^{-3}	1.28×10^4	1.16×10^4	0.90
1.5	2.92×10^5	8.23×10^{-5}	3.27×10^4	3.20×10^4	0.98
2.5	2.94×10^5	9.23×10^{-5}	2.13×10^4	2.31×10^4	1.08
7	3.34×10^5	3.04×10^{-5}	1.43×10^4	1.77×10^4	1.24

forces even as the mean contact force decreases. The coefficient of variation (COV) also increases with strain, suggesting the distribution of contact forces becomes less uniform as the specimen is sheared.

6.1.2 Bond breakage

Parallel bonds can experience either normal or shear failure modes. Figure 14 shows bond breakage evolution for the 1% cc, 2.5% cc and 5% cc cases. The total fraction of broken bonds at the end of the test are nearly the same for all three cases, but the shear bond breakage/normal bond breakage ratio increases with increasing cement content. The ratio is 1.03, 2.27 and 4.00 for 1% cc, 2.5% cc and 5% cc case respectively at $\varepsilon_a = 10\%$. For the 1% cc case, there

are almost equal chances for normal and shear bond breakage while for the 5% cc case, shear bond breakage mode dominates. This occurs because in the lower cement content specimens there are contact points that are not bonded and thus, local shear rearrangement and force redistribution can occur within the specimen without shear bond breakage. The spatial distribution of these two bond breakage modes on an x–z plane with a thickness of $2.5 \times D_{50}$ passing through the specimen axis of symmetry is demonstrated in Fig. 15. No particular distribution pattern is seen for each bond breakage mode. Breakage events are uniformly distributed within the shear bands with an increasing concentration of shear bond breakage points as the cement content increases. It is found that although the onset of bond breakage occurs at almost the same strain level for different cement contents, its
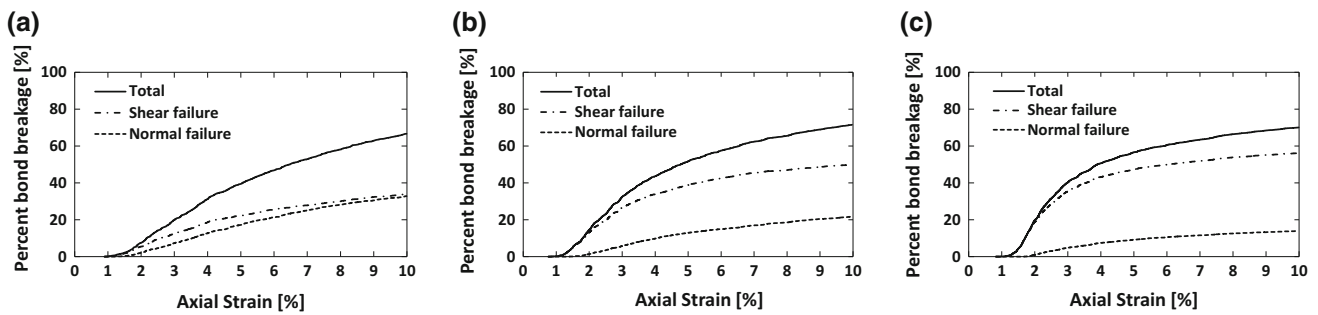
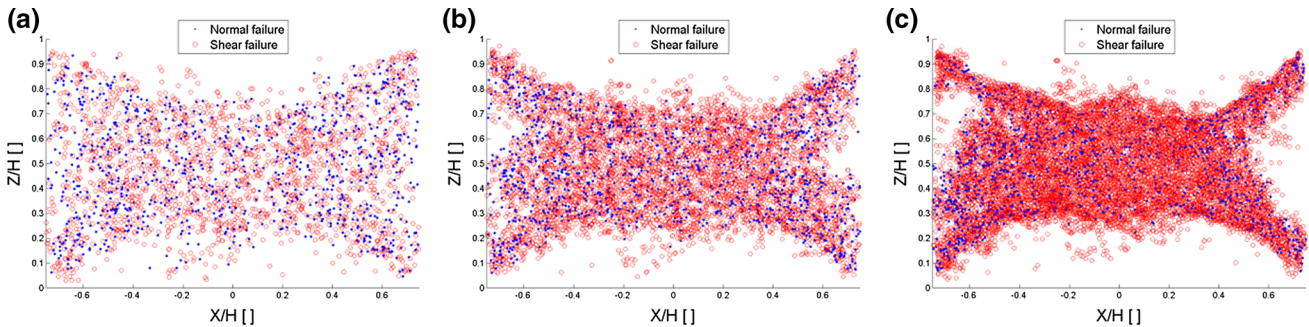**Fig. 14** Bond breakage evolution during triaxial compression. **a** 1% cc; **b** 2.5% cc; **c** 5% cc

Fig. 15 Spatial distribution of bond breakage at $\varepsilon_a = 10.0\%$: **a** 1% cc; **b** 2.5% cc; **c** 5% cc (*circle marker* shear failure; *point marker* normal failure)

development becomes more 'brittle' as the cement content is increased.

6.1.3 Void ratio and coordination number

Mesoscale (i.e., particle neighborhood) void ratio and coordination number were measured in hundreds of random locations within the specimen. The evolution of average void ratio and coordination number are shown in Fig. 16. The void ratio first slightly decreases, suggesting an initial contractive volumetric change, and then increases and approaches a steady state at approximately $\varepsilon_a = 6.0\%$. It shows a similar trend as the evolution of volumetric strain versus axial strain as computed from boundary measurements and shown in Fig. 12. The decrease in coordination number reflects a dilative response in general but it reaches a steady state at a lower global axial strain level than void ratio. The same trend was also observed by Rothenburg and Kruyt [33]. This is not surprising as there is no unique relationship between void ratio and coordination number. In fact, the rigid balls with soft contacts used in this study allow increase in volume with no change in coordination number just by the reduced overlap between two particles in contact. In addition, Rothenburg and Kruyt [33] stated that critical void ratio cannot be quantified just by critical coordination number but also by a unique *critical anisotropy*. As discussed in the next section, at 3%
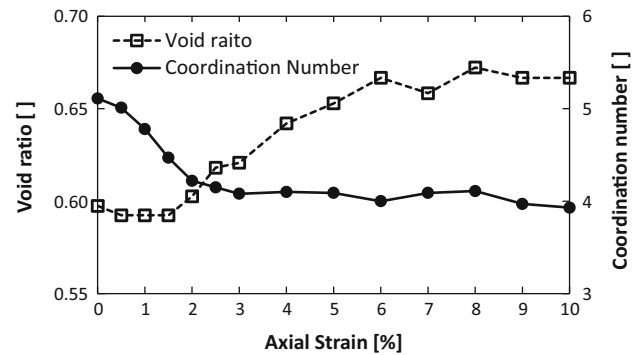

Fig. 16 Evolution of void ratio and coordination number for 5% cc specimen during triaxial compression

axial strain the coordination number is at critical state but contact anisotropy is still evolving.

6.1.4 Anisotropy evolution

To further investigate the difference in response of uncemented and cemented assemblies at the microscale level, spherical histograms are used to show the distribution of orientation of contact normal vector, contact normal force, and contact shear force (Figs. 17, 18). Spherical histograms provide good firsthand information about the concentration of one parameter along some specific axis by visual observation. However, to better quantify anisotropy evolution in
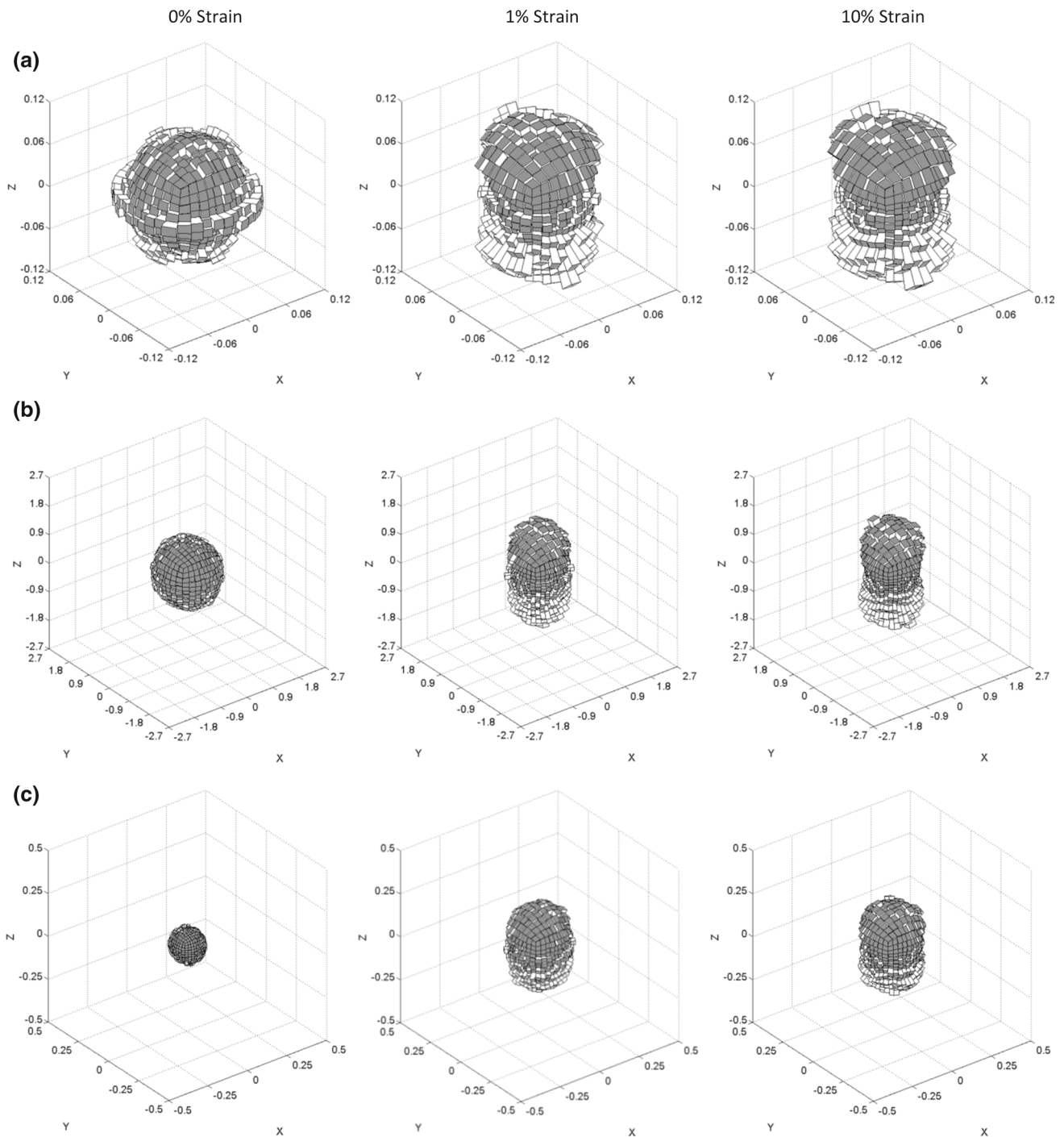
Fig. 17 3D histograms of: **a** contact orientation; **b** contact normal force orientation; **c** contact shear force orientation at 0, 1, and 10% strain values for an uncemented assembly

the assembly, the method proposed by Woodcock [46] is employed. In this method the unit normal contact vectors form a fabric tensor as follows:

$$R_{ij} = \frac{1}{N} \sum_{c \in V} n_i^c n_j^c \qquad (1)$$

where N is the total number of contacts in the assembly and n_i^c ($i = 1, 2, 3$) is the ith component of the normal vector at contact point c. This tensor possesses three eigenvalues ($\lambda_1, \lambda_2, \lambda_3$), the sum of which is equal to 1. These eigenvalues are a measure of the degree of clustering in the data about their respective eigenvectors (v_1, v_2, v_3). For exam-
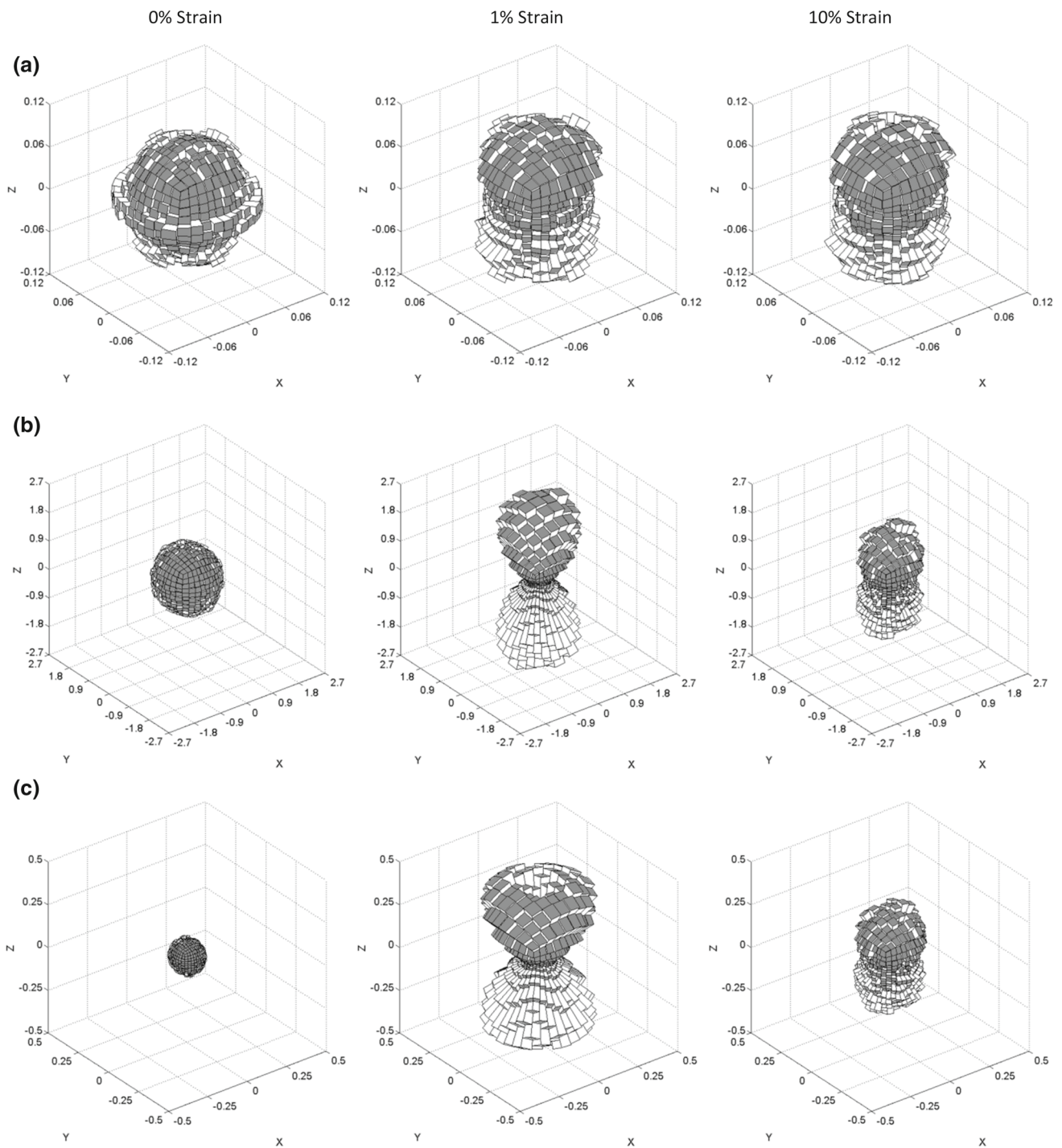
Fig. 18 3D histograms of: **a** contact orientation; **b** contact normal force orientation; **c** contact shear force orientation at 0, 1, and 10% strain values for an assembly with 5% cc

ple, $\lambda_1 = \lambda_2$ refers to axisymmetric distribution around v_3 or $\lambda_1 = \lambda_2 = \lambda_3$ refers to an equal distribution around all three eigenvectors (spherical distribution). Therefore, these eigenvalues are directly related to the fabric shape [46]. The same tensors can be calculated for normal contact forces as follows:

$$F_{ij}^n = \frac{1}{N} \sum_{c \in V} f_n^c n_i^c n_j^c \tag{2}$$

where f_n^c is the value of total normal force at contact point c. Ng [28] used eigenvalue ratios versus strain plots to study the fabric change in unbound granular assemblies subjected to

Table 4 Eigenvalues corresponding to distribution of different contact parameters around principal axes at different strains values

Cement content (%)	Contact parameter	Strain (%)	λ_y/λ_x	λ_z/λ_x	λ_z/λ_y
0	Orientation	0	1.01	1.02	1.01
		1	1.01	1.28	1.27
		10	1.01	1.31	1.30
	Normal force	0	1.02	1.04	1.02
		1	1.01	1.71	1.70
		10	1.00	1.82	1.80
5	Orientation	0	1.01	1.02	1.01
		1	1.01	1.28	1.26
		10	1.01	1.25	1.23
	Normal force	0	1.02	1.04	1.02
		1	1.01	2.78	2.75
		10	1.02	1.80	1.77

varying stress paths. In this paper, the fabric descriptors are defined as λ_y/λ_x, λ_z/λ_x, and λ_z/λ_y corresponding to main axes x, y, and z with z being the direction of application of deviatoric stress. Variations of eigenvalue ratios with axial strain are presented in Table 4 and plotted in Fig. 19. Figure 17a shows the distribution of contact orientation in the assembly. The length of each prism in the histogram is equal to the fraction of total contacts whose directions are within the solid angle subtended by the prism boundaries. According to Fig. 17a, the distribution of contact orientation after the consolidation phase is almost spherical with equal eigenvalue ratios (Table 4). At 1% strain, the histogram elongates in the z-direction due to the dissolution of contacts normal to the z-axis, resulting in the preferential contact orientation shown. These preferentially oriented contacts then form the strong force network [32] in the z-direction and resist the external applied load on the assembly. Contact orientation of the assembly at 10% strain is similar to that at 1% strain and has the same eigenvalue ratios. This implies no considerable rotation of particles occurs from 1 to 10% strain. Figure 17b shows the distribution of contact normal force. The length of each prism in the histogram is equal to the sum of contact normal forces whose orientations are within the solid angle subtended by the prism boundaries normalized by the average contact normal force in the assembly. The distribution under isotropic confining stress is spherical, as expected for spherical particles [6]. At 1% strain, the histogram elongates in the z-direction and the eigenvalue ratio (λ_z/λ_x) increases from 1.04 to 1.71. At 10% strain, the histogram has not changed size in the z-direction, but has shrunk laterally, leading to a larger anisotropy in the assembly ($\lambda_z/\lambda_x = 1.82$). The distribution of contact shear force is shown in Fig. 17c. The length of each prism in the histogram is equal to the sum of contact shear forces whose contact normal vectors are oriented within the solid angle subtended by the prism boundaries normalized by the average contact normal force

in the assembly. Contact shear forces are very small and their distribution is spherical under isotropic confining stress, indicating low locked-in shear forces and a high degree of homogeneity post-consolidation. Anisotropy increases constantly with increasing strain. Both histograms at 1 and 10% strains enlarge considerably compared to the consolidation phase which implies that the contact shear forces in the assembly are increased substantially (again, there is very little locked-in shear after consolidation). In general, the difference between the histograms at 1 and 10% strain is not very appreciable as the two points being considered include one immediately before maximum shear strength and the other in the steady state zone of a sample exhibiting loose behavior (Fig. 6a).

Histograms of a cemented assembly with 5% cc are shown in Fig. 18. The uncemented and cemented assemblies are identical prior to the installation of bonds in the cemented assembly, so all three histograms at 0% global axial strain are also identical for both specimens. When comparing contact orientation alone, Figs. 17a and 18a indicate very little difference across strain levels with nearly equal eigenvalue ratios. This is consistent with Fig. 19a where anisotropy values of uncemented and cemented specimens are very similar for 1 and 10% axial strains although anisotropy evolution is different for both specimens.

Figure 18b shows that at 1% strain, contact normal forces have both a larger value and a larger degree of anisotropy when compared to the uncemented assembly. The eigenvalue ratio increases from 1.71 for uncemented specimen to 2.78 for cemented specimen. The increased normal forces are due to the bonding at the contact points, which increase contact stiffness and thus result in greater contact forces at the same displacement relative to the unbonded assembly. At 10% strain, where about 70% of parallel bonds have already failed (Fig. 12c), the reduction of normal stiffness at contact points results in a decrease of contact normal forces. At this
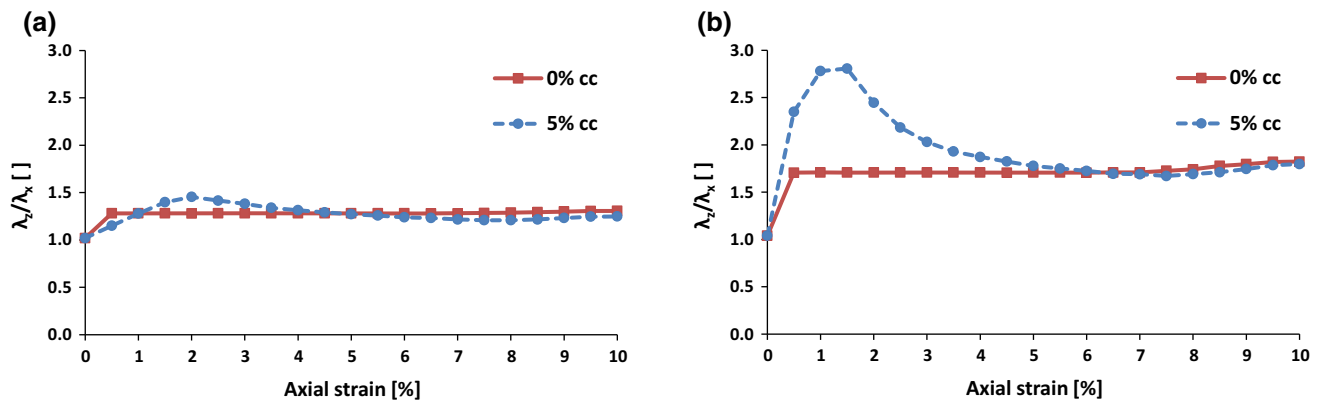
Fig. 19 Anisotropy evolution for **a** contact orientation; **b** contact normal force

level of strain, both cemented and uncemented histograms are much the same in terms of size and anisotropy (refer to Table 4).

Comparing Figs. 17c and 18c, the shear contact force histograms for the cemented assembly are clearly larger than those for the uncemented assembly. This is due to two complimentary mechanisms: (1) the increased shear stiffness at contacts points leading to increased shear forces, much like in the case of the normal forces; and (2) bonds that allow the contact points to support a greater force prior to slip relative to the unbonded case. The direction of the maximum shear forces—which are potential shear failure planes—can be observed in Fig. 18c for 1% strain. This preferential shear force orientation is consistent with the dilatant response (shown in Fig. 12) and post-failure geometry of the assembly, which clearly exhibits strain localization. Moving towards 10% strain, the shear force histogram gets smaller in both size and anisotropy. This indicates the presence of smaller and more uniform shear forces in the assembly after breakage of a significant number of the bonds.

Considering the variation of eigenvalue ratio with axial strain (Fig. 19), both contact orientation anisotropy and contact normal force anisotropy of uncemented specimen initially increase and then are approximately constant for the remainder of the simulation. For the cemented assembly, the same parameters first increase to a maximum value before decreasing to steady state, similar to the anisotropy behavior of a dense uncemented assembly [33]. The difference between degree of anisotropy of cemented and uncemented specimens is more pronounced for contact normal force as contact points in the cemented specimen are able to carry larger normal forces before the bonds break (i.e., before slippage occurs at the contact). Figure 19 also demonstrates existence of a *critical anisotropy* independent of cement content that was also reported by Rothenburg and Kruyt [33] for uncmented granular assemblies independent of initial state.

From these microscale observations, it is found that for weakly cemented particulate assemblies (e.g. soils), shear

band formation, force-chain evolution and volumetric dilation are all closely related to cement degradation. At low strain levels, the bond network is intact so all particles can jointly share the load resulting in a uniform contact force distribution. As strain increases, the initial bond breakage is mild and random. Interparticle slippage is hindered by the bonding effect, and thus, the shear strength is improved compared to uncemented case. Strong force-chains are formed, carrying most of the load. When the strain is further increased, intensive bond breakage occurs, which leads to the formation of 'X' shaped shear bands. With less interparticle bond resistance inside the shear band, contact forces are concentrated in the force-chains. Weak points are established which results in local force-chain buckling. Inside the developing shear bands, clusters of still-bonded particles can rotate to form particle arches to withstand the concentrated contact force and also contribute to the volumetric dilation, which is demonstrated by the increased local porosity. When the strain level reaches the steady state, shear bands stop expanding and separate the bond network into several intact zones. High contact forces are locked in the central area. The stability of the open voids inside the shear band is maintained through stress arching. Particle rotation and volumetric dilation are prohibited outside the shear band where contact forces are low and the bond network is preserved. Similar observations on the evolution of bond breakage and force chains under shearing were reported in previous two-dimensional DEM biaxial test simulations on cemented assemblies [19,43,44]. However, the fundamental differences between the load-carrying mechanisms in cemented and uncemented specimens—particularly, the partitioning of fabric and force—have not been previously reported.

6.2 Wave propagation during shear

Cementation effects on wave propagation during triaxial compression were studied by measuring S-wave velocity at different axial strains, similar to the experimental work by
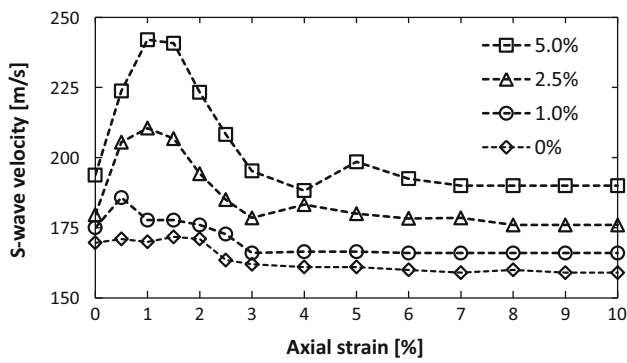
Fig. 20 Variation of S-wave velocity with axial strain during triaxial compression

Sharma et al. [39]. Figure 20 shows the measured S-wave velocity versus axial strain for uncemented, 1% cc, 2.5% cc and 5% cc specimens. The overall trends are consistent with those reported by Sharma et al. [39] based on results from physical experiments. The S-wave velocity increased during shear to a peak value and then gradually decreased with axial strain to a steady state value. Higher cement content resulted in higher S-wave velocities at all strain levels and a more distinct peak in the curve. The S-wave velocities at steady state were identical to those at initial state for 2.5% cc and 5% cc case but were lower than initial values for the 1% cc and uncemented cases. However, Sharma et al. [39] report S-wave velocities at steady state significantly lower than those at initial state for high cement contents.

Figure 12a, d shows that the peak S-wave velocity in the 5% cc specimen occurred prior to full mobilization of shear strength, consistent with results from physical experiments

[39]. Specifically, peak S-wave velocity was found to occur at the onset of bond breakage, validating the hypothesis by Sharma et al. [39] that "this phenomenon is an indicator for bond breakage and de-structuring in the samples."

Figures 21 and 22 show the evolution of shear strain on the x–z plane during S-wave propagation in the 5% cc specimen when $\varepsilon_a = 0\%$ and $\varepsilon_a = 7\%$ respectively. Recall that at $\varepsilon_a = 0\%$, the bond network was intact and the contact force nearly uniformly distributed. At $\varepsilon_a = 7\%$, an 'X' shaped bond breakage zone and strong force-chains were formed. Figure 22 demonstrates how these differences in microstructure can significantly alter wave propagation. It is clear that the S-wave propagates preferentially through the breakage zone, where the contact force-chains were formed [34,35].

In summary, the observed shear wave velocity changes for a cemented specimen can be explained as follows: With an increase of axial strain and before failure of parallel bonds, large contact forces are generated within the assembly, as shown in Fig. 13. These large contact forces increase the overlap between particles which, in turn, increases normal and shear contact stiffness:

$$k_n = \frac{2G_g\sqrt{2R}}{3\left(1 - \nu_g\right)}\sqrt{U} \tag{3}$$

$$k_s = 2\frac{\sqrt[3]{3G_g^2\left(1 - \nu_g\right)R}}{2 - \nu_g}\sqrt[3]{F_n} \tag{4}$$

where U is the overlap of the two particles, F_n is the normal contact force, R is the average radius of the two particles, and G_g and ν_g are the shear modulus and Poisson's ratio of the two particles, respectively. This results in an increase of shear
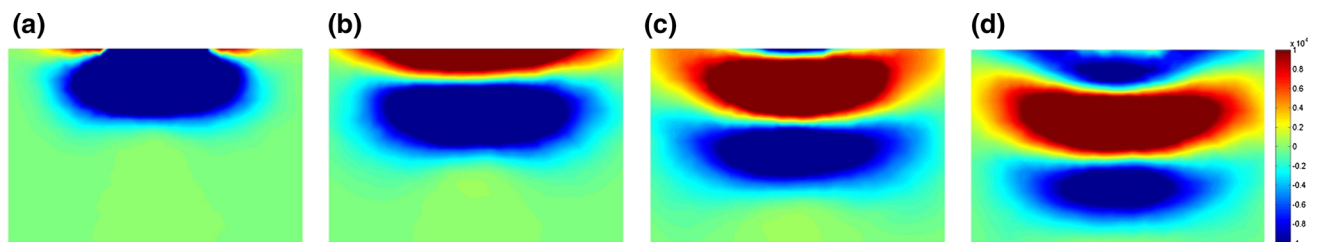

Fig. 21 Evolution of shear strain on x–z plane during S-wave propagation at **a** 10 ms; **b** 15 ms; **c** 20 ms; **d** 25 ms after excitation for 5% cc specimen at $\varepsilon_a = 0\%$ during triaxial compression
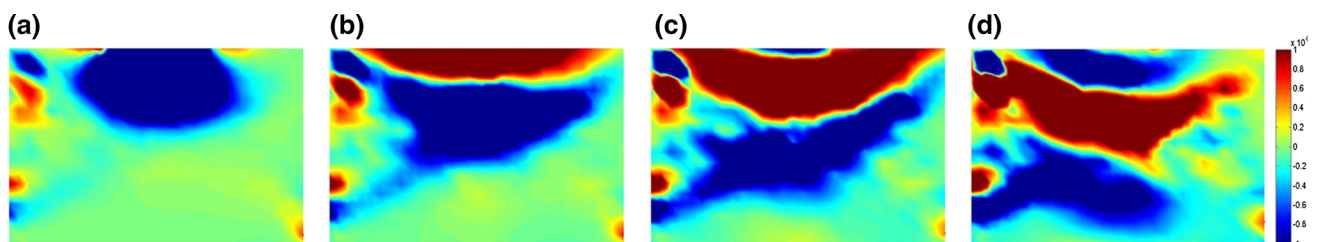

Fig. 22 Evolution of shear strain on x–z plane during S-wave propagation at **a** 10 ms; **b** 15 ms; **c** 20 ms; **d** 25 ms after excitation for 5% cc specimen at $\varepsilon_a = 7\%$ during triaxial compression

wave velocity of the assembly. With further increase of axial strain and the initiation of bond breakage, large contact forces and therefore the main pathways for shear wave propagation concentrate in a central portion of the specimen. Moreover, the average normal contact force in the assembly is reduced (Table 3). These two phenomena together result in a decrease in shear wave velocity.

At the macroscale level, shear wave velocity is shown to be a function of effective confining stress [35,47]. More specifically, Ning et al. [30] showed that for a granular assembly the shear wave velocity is constant for the same mean effective stress for both isotropic and K_0 conditions. In an axisymmetric compression test with radial stress held constant, the mean effective stress increases with an increase in deviatoric stress and vice versa. Therefore, in zone II (Fig. 12) with the largest deviatoric stress, the largest shear wave velocity is expected.

7 Summary and conclusions

The parallel bonding model can be used in DEM simulations to effectively reproduce many of the characteristics present in cemented soils and observable at the element scale. It was observed in the present work that the peak shear strength is significantly improved as the cement content is increased. Meanwhile, the stress–strain response becomes more brittle and the volumetric strain becomes more dilative. The S-wave velocity (small-strain stiffness) increases when the cement content is increased and decreases as decementation occurs.

Under isotropic confinement, S-wave velocity increases as the cement content is increased (for a given isotropic confining stress). For a specimen with a given cement content, S-wave velocity increases as the confining stress is increased, following the typical power law relationship. The difference between the S-wave velocities measured from the specimens with load-before-cementing (LBC) and cementing-before-loading (CBL) cement-stress histories is small. However, the S-wave velocities of LBC specimens are less sensitive to the change of stress state, likely due to larger contact areas being formed when particles are loaded without cement, resulting in a stiffer contact behavior. The distinctions between the LBC and CBL cases are revealed from a microscale investigation. It is shown that the contact forces for the CBL cases are more uniformly distributed compared to the LBC cases. For the LBC cases under high isotropic confining stress, particle arches are formed surrounding the core of the specimen, resulting in relatively high porosity and low coordination number inside the zone surrounded by particle arches.

For numerical specimens subjected to axisymmetric compression, the simulations indicate that stress–strain and volumetric response are closely correlated to bond breakage. The onset of bond breakage corresponds to a yield point in the stress–strain curve and the transition from volumetric contraction to volumetric dilation. Complimentary shear bands are formed on a cutting plane as axial strain increases. Inside the shear band, large bond breakage occurs and the normal contact forces are concentrated, accompanied by high local porosity and low local coordination number. Outside the shear band, the bond network remains intact and less change in local porosity and local coordination number can be seen. The bond breakage is primarily due to shear failure in the high cement content case. More normal mode bond failure is seen for low cement content cases.

Contact orientation, normal force orientation, and shear force orientation anisotropy were observed to evolve differently for cemented and uncemented assemblies. In heavily cemented specimens, the predominant load-bearing mechanism prior to significant bond breakage is through increased contact normal forces along the axis of deviatoric loading and increased contact shear forces on planes oriented at 45° relative to the axis of deviatoric loading (Figs. 17, 18). In lower cement content specimens, the unbonded contact points allow for local shear rearrangement and force redistribution within the specimen without shear bond breakage, resulting in a fundamentally different failure mechanism when compared to uncemented or heavily cemented specimens (Figs. 14, 15). Anisotropy evolution in terms of contact orientation and normal contact force is different for cemented and uncemented specimens; however, there is a unique critical anisotropy at large axial strain regardless of cementation level.

The evolution of S-wave velocity agrees with the corresponding experimental results [39]. S-wave velocity first increases to a peak value then decreases to a stable value. The peak S-wave velocity occurs before the peak shear stress is reached, which corresponds to the onset of bond breakage. The shear strain contours on a cutting plane clearly show that the S-wave propagates preferably through the bond breakage zone, where the contact forces are concentrated. However, two significant differences were observed between numerical and physical S-wave velocities in cemented assemblies: (1) numerical assemblies were much less sensitive to increasing bulk stress than physical assemblies; and (2) the presence of parallel bonds does not increase S-wave velocity as much as would be expected based on physical experiments. This latter point also manifests in terms of the magnitudes of pre- and post-failure S-wave velocities observed in axisymmetric compression (Fig. 20). These observations are likely due to the fact that parallel bonds are a mathematical construct that serve to increase normal and shear resistance at a contact but do not increase the contact area between particles. In real soil, the effective contact area is increased in the presence of a cementing agent. This is a topic that is currently the subject of active research, including a recent paper [45] that proposes a constitutive model that considers this effect.

Compliance with ethical standards

Conflict of interest We have no potential conflict of interest.

References

1. Acar, Y.B., El-Tahir, A.E.: Low strain dynamic properties of artificially cemented sand. J. Geotech. Eng. **112**, 1001–1015 (1986)
2. Baig, S., Picornell, M., Nazarian, S.: Low strain shear moduli of cemented sands. J. Geotech. Geoenviron. Eng. **123**(6), 540–545 (1997)
3. Brandt, H.: Study of speed of sound in porous granular media. ASME Trans. J. Appl. Mech. **22**(4), 479–486 (1955)
4. Chang, C.S., Misra, A., Sundaram, S.S.: Properties of granular packings under low amplitude cyclic loading. Soil Dyn. Earthq. Eng. **10**(4), 201–211 (1991)
5. Chang, T.S., Woods, R.D.: Effect of particle contact bond on shear modulus. J. Geotech. Eng. **118**(8), 1216–1233 (1992)
6. Chantawarangul, K.: Numerical Simulations of Three-Dimensional Granular Assemblies. PhD Thesis, University of Waterloo, Ontario, Canada (1993)
7. DeJong, J.T., Fritzges, M.B., Nusslein, K.: Microbially induced cementation to control sand response to undrained shear. J. Geotech. Geoenviron. Eng. **132**(11), 1381–1392 (2006)
8. Duffy, J., Mindlin, R.D.: Stress-strain relations and vibrations of granular medium. ASME Trans. J. Appl. Mech. **24**(4), 585–593 (1957)
9. Evans, T.M., Frost, J.D.: Multiscale investigation of shear bands in sand: physical and numerical experiments. Int. J. Numer. Anal. Methods Geomech. **34**(15), 1634–1650 (2010)
10. Evans, T.M., Lee, J., Yun, T.S., Valdes, J.R.: Effective thermal conductivity in granular mixtures: numerical studies. In: Fifth International Symposium on Deformation Characteristics of Geomaterials, Seoul, Korea, IS-Seoul, pp. 815–820 (2011)
11. Evans, T.M., Ning, Z.: Wave Propagation in Assemblies of Cemented Spheres. In: Powders and Grains 2013: Proceedings of the 7th International Conference on Micromechanics of Granular Media, American Institute of Physics, vol. 1542(1), pp. 233–236 (2013)
12. Evans, T.M., Khoubani, A., Montoya, B.M.: Simulating mechanical response in bio-cemented sands. In: Oka, F., Murakami, A., Uzuoka, R., Kimoto, S. (eds.) Computer Methods and Recent Advances in Geomechanics, pp. 1569–1574. CRC Press, Boca Raton (2014)
13. Evans, T.M., Zhao, X.: A discrete numerical study of the effect of loading conditions on granular material response/IS-Atlanta. In: Fourth International Symposium on Deformation Characteristics of Geomaterials, Atlanta, GA, September 22–24 (2008)
14. Fazekas, S., Török, J., Kertész, J., Wolf, D.E.: Morphologies of three-dimensional shear bands in granular media. Phys. Rev. E **74**(3), 031303 (1–6) (2006)
15. Fernandez, A., Santamarina, J.C.: The effect of cementation on the small strain parameters of sands. Can. Geotech. J. **38**(1), 191–199 (2001)

16. Goddard, J.D.: Nonlinear elasticity and pressure-dependent wave speeds in granular media. Proc. R. Soc. Lond. A Math. Phys. Sci. **430**(1878), 105–131 (1990)
17. Hardin, B.O., Richart, J.F.E.: Elastic wave velocities in granular soils. ASCE Proc. J. Soil Mech. Found. Div. **89**(SM1, Part 1), 33–65 (1963)
18. Itasca.: PFC3D: Particle Flow Code in 3 Dimensions. 4.0 (2009)
19. Jiang, M., Zhang, W., Sun, Y.: An investigation on loose cemented granular materials via DEM analyses. Granul. Matter **15**, 65–84 (2013)
20. Johnson, K.L.: Contact Mechanics. Cambridge University Press, Cambridge (1985)
21. Kuwabara, G., Kono, K.: Restitution coefficient in a collision between two spheres. Jpn. J. Appl. Phys. **26**(8), 1230–1233 (1987)
22. Lade, P.V., Overton, D.D.: Cementation effects in frictional materials. J. Geotech. Eng. **115**, 1373–1387 (1989)
23. Landau, L.D., Lifshitz, E.M.: Theory of Elasticity. Pergamon, New York (1970)
24. Lee, J., Santamarina, J.C.: Bender elements: performance and signal interpretation. J. Geotech. Geoenviron. Eng. **131**(9), 1063–1070 (2005)
25. Mitchell, J.K., Soga, K.: Fundamentals of Soil Behavior, 3rd edn. Wiley, New York (2005)
26. Mohsin, A.K.M., Airey, D.W.: Automating G_{max} measurement in triaxial tests. Deformation Characteristics of Geomaterials IS Lyon, Taylor & Francis, Lyon, France, pp. 73–80 (2003)
27. Montoya, B.M., DeJong, J.T., Boulanger, R.W.: Dynamic response of liquefiable sand improved by microbial-induced calcite precipitation. Géotechnique **63**(4), 302–312 (2013)
28. Ng, T.T.: Discrete element simulation of the critical state of a granular material. Int. J. Geomech. **9**(5), 209–2016 (2009)
29. Ning, Z., Evans, T.M.: Discrete element method study of shear wave propagation in granular soil. In: Proceedings of the 18th International Conference on Soil Mechanics and Geotechnical Engineering, France, Paris, pp. 1031–1034 (2013)
30. Ning, Z., Khoubani, A., Evans, T.M.: Shear wave propagation in granular assemblies. Comput. Geotech. **69**, 615–626 (2015)
31. Potyondy, D.O., Cundall, P.A.: A bonded-particle model for rock. Int. J. Rock Mech. Min. Sci. **41**(8), 1329–1364 (2004)
32. Radjai, F., Wolf, D.E., Jean, M., Moreau, J.: Bimodal character of stress transmission in granular packings. Phys. Rev. Lett. **80**(1), 61–64 (1998)
33. Rothenburg, L., Kruyt, N.P.: Critical state and evolution of coordination number in simulated granular materials. Int. J. Solids Struct. **41**(21), 5763–5774 (2004)
34. Sadd, M.H., Adhikari, G., Cardoso, F.: DEM simulation of wave propagation in granular materials. Powder Technol. **109**(1–3), 222–233 (2000)
35. Santamarina, J.C., Klein, K., Fam, M.: Soils and Waves. Wiley, Chichester (2001)
36. Saxena, S.K., Lastrico, R.M.: Static properties of lightly cemented sand. J. Geotech. Eng. Div. **104**(12), 1449–1465 (1978)
37. Saxena, S.K., Avramidis, A.S., Reddy, K.R.: Dynamic moduli and damping ratios for cemented sands at low strains. Can. Geotech. J. **25**(2), 353–368 (1988)
38. Schnaid, F., Prietto, P., Consoli, N.: Characterization of cemented sand in triaxial compression. J. Geotech. Geoenviron. Eng. (2001). doi:10.1061/(ASCE)1090-0241(2001)127:10(857)
39. Sharma, R., Baxter, C., Jander, M.: Relationship between shear wave velocity and stresses at failure for weakly cemented sands during drained triaxial compression. Soils Found. **51**(4), 761–771 (2011)
40. Sitharam, T.G., Vinod, J.S., Rothenburg, L.: Shear behavior of glass beads using DEM. In: Powders and Grains, pp. 257–260 (2005)
41. Trent, B.C., Margolin, L.G.: Modeling fracture in cemented granular materials. Fracture Mechanics Applied to Geotechnical Engi-

neering (ASCE Publications. Proc, ASCE National Convention, Atlanta) (1994)

42. Walton, K.: The effective elastic moduli of a random packing of spheres. J. Mech. Phys. Solids **35**(2), 213–226 (1987)

43. Wang, Y.H., Leung, S.C.: A particulate-scale investigation of cemented sand behavior. Can. Geotech. J. **45**, 29–44 (2008)

44. Wang, Y.H., Leung, S.C.: Characterization of cemented sand by experimental and numerical investigations. J. Geotech. Geoenviron. Eng. **134**(7), 992–1004 (2008)

45. Weuster, A., Strege, S., Brendel, L., Zetzener, H., Wolf, D.E., Kwade, A.: Shear flow of cohesive powders with contact crystallization: experiment, model and calibration. Granul. Matter **17**(2), 271–286 (2015)

46. Woodcock, N.H.: Specification of fabric shapes using an eigenvalue method. Geol. Soc. Am. Bull. **88**, 1231–1236 (1977)

47. Yanagisawa, E.: Influence of void ratio and stress condition on the dynamic shear modulus of granular media. In: Jenkins, J.T., Satake, M. (eds.) Advances in the Mechanics and Flow of Granular Materials, pp. 947–960. Elsevier, Amsterdam (1983)

48. Yang, J., Gu, X.Q.: Shear stiffness of granular material at small strains: does it depend on grain size. Géotechnique **63**(2), 165–179 (2012)

49. Yun, T.S., Santamarina, J.C.: Decementation, softening, and collapse: changes in small-strain shear stiffness in K_0 loading. J. Geotech. Geoenviron. Eng. **131**(3), 350–358 (2005)

50. Yun, T.S., Evans, T.M.: Three-dimensional random network model for thermal conductivity in particulate materials. Comput. Geotech. **37**(7–8), 991–998 (2010)

51. Zhao, X., Evans, T.M.: Discrete simulations of laboratory loading conditions. Int. J. Geomech. **9**(4), 169–178 (2009)